Facile synthesis of photoactive CuO-ZrO₂ nanoparticles for photocatalytic degradation of both cationic and anionic dyes

K. Rajput ^{a,b}, V. Diniz ^b, S. Sharma ^c, C. R. Crick ^b, M. D. Sharma ^{a,*}

Although many photocatalysts have been explored, their complex synthesis often limits practical use. This study presents a simple method to synthesize CuO-ZrO₂ nanocatalysts (~10 nm), effective in degrading both cationic (Bismarck Brown Y) and anionic (Reactive Black 5) dyes. The catalyst synthesised at pH 7 showed the best properties- highest pore volume (0.124 cc/g), 2.4 eV band gap, and removal efficiencies of ~92.5% for RB and ~76.4% for BB. Optimal degradation pH varied by dye. Trapping studies confirms electrons and holes as main active species. A Vigna radiata germination assay confirmed the material's non-toxic nature, supporting its environmental safety and applicability.

(Received June 19, 2025; Accepted September 24, 2025)

Keywords: Photocatalysis, Transition metal, Nanoparticles, Reactive black, Bismarck brown, Dye degradation, Water treatment, Ecotoxicological assay

1. Introduction

Water contamination is overwhelmingly accompanied by numerous detrimental effects and is an environmental issue with growing prevalence. This has prompted numerous research endeavours aimed at addressing this global crisis by developing advanced materials for water purification [1]–[3]. Amidst water contaminants, the extensive production of organic dyes for multifarious purposes has sparked concerns regarding their prominent presence in industrial wastewater. The substantial discharge of these dyes is recognized as a major source of organic pollution in aquatic environments, which is characterized by their high potential for toxic aromatic amines and long persistence times [4].

Azo dyes, commonly utilized in the textile sector for their versatility and low cost, are a vital component of many commercial dying solutions, accounting for nine million tonnes (> 70%) of global manufacturing [5] needs. Nonetheless, they are also among the most hazardous synthetic dyes due to their recalcitrant properties, thereby posing a substantial threat to the environment [6]. In aquatic ecosystems, dyes elevate biochemical and chemical oxygen demands (BOD/COD), while impeding photosynthesis, thereby hindering plant growth [7]. Moreover, they can accumulate, bio magnify, and infiltrate food webs, contributing to carcinogenic effects and further threatening environmental and human health [8],[9]. Reactive Black (RB) and Bismarck Brown (BB) are widely used azo dyes currently employed across diverse industry sectors such as textiles, printing, and cosmetics [10], [11]. Given their widespread use and representation of both cationic and anionic dyes, RB and BB were adopted in this study as model contaminants to assess the efficiency of dye removal.

With the growing issue of water scarcity, considerable attention has been directed toward the removal of dyes from water sources [12]. Much of this research focuses on the adsorption and chemical breakdown of these contaminants to improve water quality [13]. This includes the use of chemical and biological agents in nanomaterials [14], [15] aimed to improve water treatment

^a Department of Physics, Panjab University, Chandigarh, 160014, India

^b School of Engineering and Materials Science, Queen Mary University of London, E1 4NS, London, UK

^c Department of Cytology and Gynecological Pathology, Post Graduate Institute of Medical Education & Research, Chandigarh, 160012, India

^{*} Corresponding author: manishdevsharma@yahoo.com https://doi.org/10.15251/DJNB.2025.203.1135

processes [16]. The use of transition metal-based nanomaterials has been a recent area of intense investigation in heterogeneous photocatalysis [17], [18]. These materials are utilized as they are generally effective and dependable photocatalysts, providing a sustainable and dynamic alternative to other methods available [19], while purifying water bodies through the mineralization of contaminants under UV or visible light [20]. The key advantages of these nanostructured materials are their high performance, low cost (both upfront and ongoing), effective applicability, and minimized toxicity [17]. In recent years, numerous advancements have been documented in the field of photocatalysts, both with [21]or without [22] metal-based catalysts, demonstrating reduced recombination rates [23] and enhanced contaminant removal efficiency. However, the frequent reliance on multistep synthesis processes remains a major drawback, hindering the scalability and broader application of these technologies.

Among photocatalysts, CuO-ZrO₂ nanocomposites have recently been proposed as highly efficient materials for water remediation, positioning them as a promising solution for wastewater purification [24], [25]. Their high surface area, provided by zirconia nanoparticles, offers ample active sites for dye adsorption, enhancing the interaction time between the dye and the photocatalyst, thereby significantly improving the photocatalytic activity [26]. Additionally, the synergistic between CuO and ZrO₂ nanoparticles further enhances this performance due to several key factors: (i) stabilization of various oxidation states of Cu by ZrO₂, which improves the redox properties of the materials; (ii) the interaction between CuO and ZrO2 at their interfaces, which creates new active sites; and (iii) the combination of these nanoparticles, which enhances light absorption and charge separation, leading to the generation of more photogenerated electrons and holes available for photocatalytic reactions. These combined effects result in a markedly improved photocatalytic performance compared to the individual components and these materials therefore demonstrate excellent chemical stability, ensuring durability during dye degradation reactions [27]-[29] Despite their significant potential for real-world applications, the widespread use of CuO-ZrO₂ nanocomposite is hindered by the synthetic protocols commonly reported in the literature, which often require high temperatures, multistep processes, and extended reaction times, as shown in Table S1 (see supporting information). These limitations reduce their scalability and practicality for large-scale implementation.

The present research aims to address the limitations of traditional synthesis methods by developing a more straightforward approach for synthesizing CuO-ZrO₂ nanocomposites. For that CuO-ZrO₂ nanocomposites were synthesized by a single-step method, and their photocatalytic activity was assessed for the removal of model dye molecules: cationic BB and anionic RB dyes. The effect of various experimental conditions on the removal of the dyes has been examined, including: catalyst loading, dye concentration, pH, and time. Additionally, the ecotoxicological impact of the nanocomposites on *Vigna radiata* was investigated to assess its environmental safety. The novelty of the research work lies in the efficiency of the prepared photocatalyst to efficiently target and remove both the cationic and anionic dyes simultaneously under visible light, without the requirement of any arduous setup or conditions. This demonstrates the potential for a more accessible and efficient solution for wastewater treatment.

2. Materials and method

2.1. Chemicals

Copper (II) chloride dihydrate ($CuCl_2.2H_2O$), zirconium Oxychloride ($ZrOCl_2.8H_2O$) (purity, 99.98%), ammonium hydroxide solution (NH_4OH) (28.0-30.0% NH_3 basis), hexadecyltrimethylammonium bromide (CTAB) (purity, > 98%), Reactive Black 5 dye and Bismarck Brown Y (purity >97.0%) dye was purchased from Sigma-Aldrich (India). No further purification of the reagents was carried out, and they were used as purchased. All the solutions were prepared in double-distilled water.

2.2. Photocatalyst synthesis

Typically, 10 mg of CTAB was dissolved in 20 ml of distilled water under magnetic stirring for 20 min, then the precursors - 500 mg of each ZrOCl₂.8H₂O and CuCl₂.2H₂O were

dissolved under continuous stirring and kept overnight at 40 °C. As the initial pH of the metal salt solution was pH 1.6, ammonium hydroxide was introduced dropwise until the target pH reached (pH 3, 7 and 10) for individual batches respectively. In all the cases, blue precipitates were formed once the pH was adjusted but at pH10, a characteristic deep blue colour in the filtrate was observed possibly due to formation of soluble tetraamine Cu(II) complex instead of Cu(OH)₂ precipitates which might have leached out the amount of Cu in the pH 10 composites.

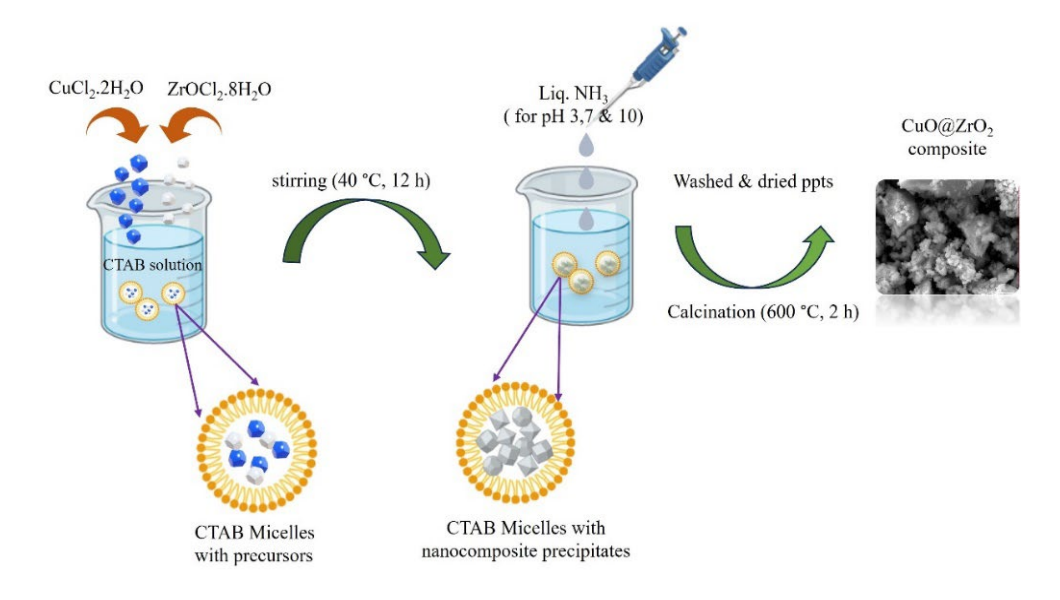


Fig. 1. Schematic showing the fabrication procedure for CuO- ZrO_2 nanocomposites at variable pH (3,7&10).

These precipitates were then separated using a centrifuge (Eppendorf microcentrifuges 5425) operating at 10,000 rpm and for 15 min. The obtained blue slurries were thoroughly washed 5 times with distilled water and lastly with ethanol in order to remove all the unreacted species. These slurries were then dried in an oven for 2 h at 50 °C and further calcinated for 2h at 600 °C each (Figure 1). The obtained samples were named as Cu/Zr(3), Cu/Zr(7) and Cu/Zr(10) according to the pH of their formation.

2.3. Photocatalyst characterization

All the prepared CuO-ZrO₂ nanocomposites (Cu/Zr(3), Cu/Zr(7) and Cu/Zr(10)) were characterized by X-ray diffraction (XRD) spectra acquired using an XRD-7000 (SHIMADZU) diffractometer utilizing a copper anode (Kα radiation). The Adsorption/desorption isotherms were obtained with nitrogen at 77 K, using a mercury porosimeter PoreMaster (Quantachrome) and surface area analyser NOVA 4200e (Quantachrome). Previously to the analysis, the materials were degassed at 150 °C in a vacuum chamber for 24 h. Further, thermogravimetric analyses (TGA) were carried out in a TGA-2950 (TA instruments) with a heating ratio of 10°C min⁻¹ under an inert atmosphere. Then, analysis of the morphological, structural and chemical composition was conducted using scanning electron microscopy (SEM) and energy-dispersive X-ray spectroscopy (EDS) using a field-emission scanning microscope (Jeol J6360 LV). Transmission electron micrographs were recorded on Jeol JEM-F200, a high-resolution Scanning Transmission Electron Microscope (HR-TEM). Lastly, to evaluate the progress of the reactions, a UV–Vis spectrophotometer (Thermoscientific Evolution 201) in the range of 300-700 nm was employed.

2.4. Photocatalytic degradation of model dyes.

Stock solutions of anionic RB and cationic BB dye were prepared by dissolving each dye individually in double-distilled water to achieve a target concentration of 1000 mg L⁻¹. Working solutions were then prepared by diluting the stock solution in double-distilled water. The

photocatalytic activities of the CuO-ZrO₂ nanocomposites were assessed by monitoring the degradation of both dye concentrations under various experiment conditions. The degradation process was carried out under visible light irradiation, facilitated by a 60 W LED lamp by HPL Electric& Power Ltd. within a range of 400-700 nm, inside an insulated photoreactor. During this experiment, specific quantities of the photocatalyst were introduced into the dye solutions, which were then continuously stirred magnetically for a predetermined duration.

Subsequently, aliquots of the dye/nanocomposites' mixtures were taken at regular time intervals. These were then subjected to centrifugation at 5000 rpm for 5 minutes to separate the nanocomposite from the solution. The resulting degraded dye solutions were then analysed using a UV–visible spectrophotometer to measure the concentration of RB and BB using their respective absorption wavelengths of 596 nm and 468 nm, respectively. The efficiency of the photocatalytic degradation was determined using Equation (1), where C_0 represents the initial concentration of the dye solution, and C_e signifies the concentration of the dye solution after undergoing photocatalytic degradation. The data was further fitted to the various kinetic models to investigate degradation kinetics [3].

Degradation Efficiency (%) =
$$\frac{(C_0 - Ce)}{C_0}$$
.100 (Equation 1)

To determine the concentration (C) of dye at a given time, one typically uses a calibration curve, which relates the absorbance to the concentration of the dye. This calibration curve is derived from measuring the absorbance of standard solutions with known concentrations and plotting these values to create a linear relationship described by the equation: Absorbance = k*Concentration+ b. Here, k is the slope and k is the y-intercept. The y-intercept b represents the baseline absorbance when the concentration is zero, and is usually taken as 0 absorbance units. To find C, the absorbance of the dye solution at time t is measured, and the calibration curve equation is rearranged to solve for (C) as follows: $C = A_t/k$, where A_t is the absorbance at time t and k is the slope of the calibration curve. This method allows for accurate determination of the dye concentration at various time points, facilitating the assessment of dye degradation over time.

Additionally, a radical trapping study was conducted, employing 2 mM isopropyl alcohol (IPA), 2 mM ascorbic acid (ASC), 2 mM potassium dichromate ($K_2Cr_2O_7$), and 2 mM ethylenediaminetetraacetate (EDTA) as scavengers. These scavengers were utilized to trap reactive oxygen species, including hydroxyl radicals (•OH) and superoxide radicals (O_2^-), the electron (e⁻) radicals, and photogenerated holes (h+) radicals, respectively [30].

2.5. Ecotoxicological assay

The phytotoxic effects of CuO-ZrO₂ nanocomposites were evaluated through a seed germination test, with a focus on root length assessment. *V. radiata* (green grams) was employed for toxicity evaluation [31]. The seeds were soaked overnight in deionized water and then placed in a constant temperature incubator set to 37°C. For each experimental condition, 10 healthy seeds were exposed to 10 mL of CuO-ZrO₂ nanocomposites at various concentrations (0 (control), 25, 50, 75 and 100 ppm) in separate glass Petri dishes. The entire setup was shielded from light to mimic the natural dark condition in the soil, and the incubator was maintained at 37°C (optimal warmth) to facilitate seed germination. After 72 h of incubation, the number and length of rootlets were measured.

3. Results and discussion

3.1. Morphological and chemical analysis

XRD analysis (shown in Figure 2) of all the synthesized CuO-ZrO₂ nanocomposites (Cu/Zr(3), Cu/Zr(7) and Cu/Zr(10)), supported the pH-dependent precipitation behaviour observed while synthesising. The XRD patterns of CuO and ZrO₂ were present in all CuO-ZrO₂ nanocomposites, albeit at apparent varying ratios due to varying pH of formation. The peak at 30.4° corresponds to the (101) plane of tetragonal ZrO₂, while the peaks at 51.2° and 60.4°

correspond to the (112) and (211) planes of tetragonal ZrO₂, respectively. This indicates that the ZrO₂ in the nanocomposite is primarily in the tetragonal phase (JCPDS card No. 050-1089) [24], [30], [32]. The peaks at 35.6° and 38.7° are attributed to the (002) and (111) planes of monoclinic CuO, respectively, signifying that the CuO present in the nanocomposite is in the monoclinic phase (JCPDS card No. 89-5895)[33][24]. Additional peaks at 66.4°, 75.3°, and 82.91° are attributed to the (311), (004), and (224) planes of tetragonal ZrO₂, respectively (JCPDS card No. 050-1089). Overall, At pH 3, a slight broader diffraction features and lower intensities of CuO peaks indicate incomplete precipitation of Cu(OH)₂ and poor crystallinity. In contrast, the sample prepared at pH 10 also showed a marked reduction in CuO peak intensities, consistent with the leaching of Cu in the form of soluble [Cu(NH₃)₄]²⁺ complexes in presence of excess NH₄OH, leading to partial loss of copper during filtration. Only in the sample prepared at pH 7 i.e. Cu/Zr(7), the formation of distinct peaks corresponding to CuO and ZrO₂ confirmed complete coprecipitation and subsequent oxide formation successfully.

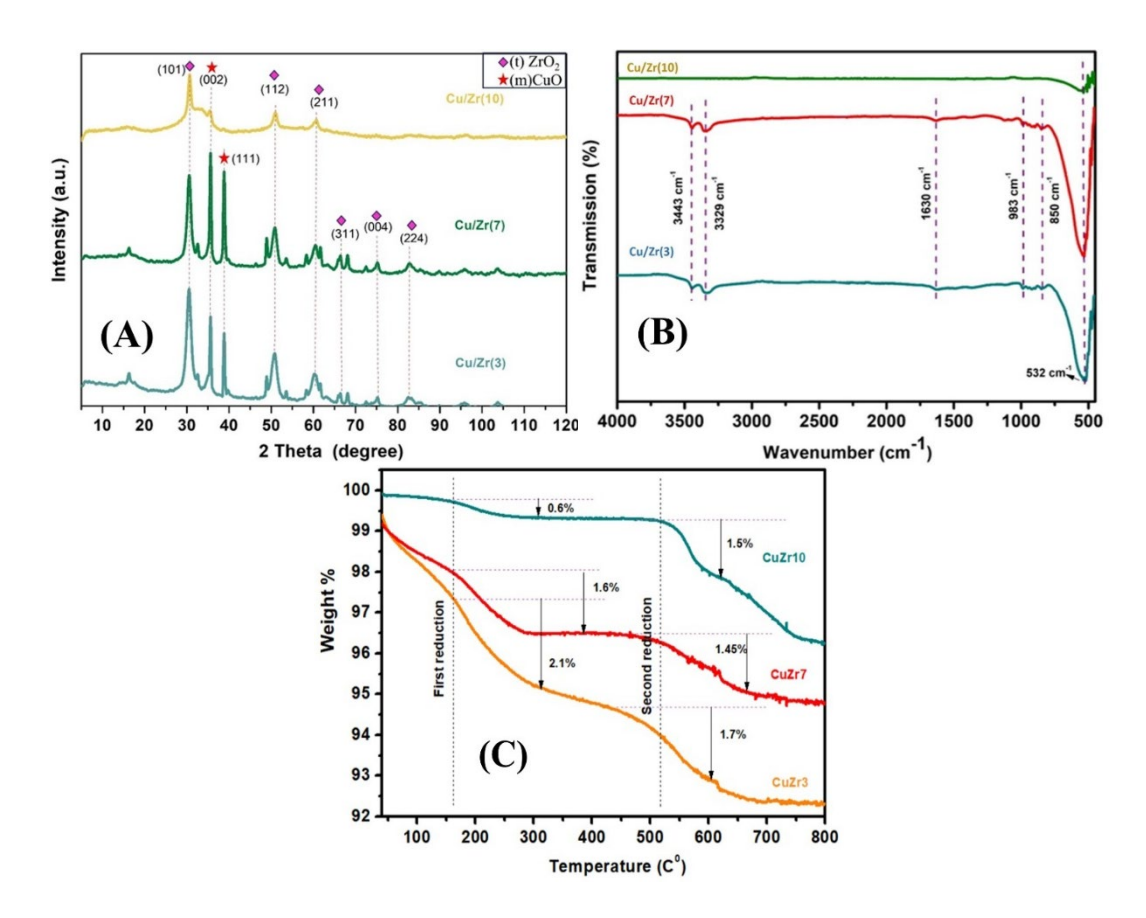


Fig. 2. (A) XRD, (B) FTIR and (C) TGA analysis of the CuO-ZrO2 nanomaterials formed at various pHs.

FT-IR spectra (Figure 2 B) of all the synthesized CuO-ZrO₂ nanocomposites provided additional insights into their composition and structure, complementing the previous XRD analysis. Several characteristic peaks were identified, corresponding to different functional groups and bond vibrations. The peaks at 3443 cm⁻¹ and 3329 cm⁻¹ are typically associated with O-H stretching vibrations. They indicated the presence of hydroxyl groups or adsorbed water on the surface of the nanocomposite, these peaks are absent in the Cu/Zr (10) due lower surface hydroxyl groups and formation of Ammonia complexes as observed in XRD results. Additionally, the slight peak at 1630 cm⁻¹ corresponds to the bending vibration (scissoring) mode of water molecules, further confirming the presence of adsorbed water on the surface of the nanocomposite Cu/Zr (3) and Cu/Zr (7) and not in Cu/Zr (10) for the same reason [24], [34], [35]. The peaks in the range 983-850 cm⁻¹ might be related to the stretching vibrations of the Zr-O bond or /a mixed mode

involving both Cu-O and Zr-O bonds, indicating an interaction [35] between the copper oxide and zirconium oxide in the nanocomposite. The peak observed at 532 cm⁻¹ is likely associated with the Cu-O stretching vibrations, indicating the presence of CuO in the nanocomposite. Notably, in the Cu/Zr(10), the peak at 532 cm⁻¹ remained less prominent, further confirming that higher pH conditions (such as pH10) might result in [Cu(NH₃)₄]²⁺ soluble complex formation and leaching of Copper at higher pH. [35], as was also indicated by the XRD data previously. Further, TGA analysis of all the synthesized CuO-ZrO2 nanocomposites has been depicted in Figure 2 C, and confirms their thermal stability and robustness of the composites. All nanocomposites were stable up to temperatures as high as 500 °C where the primary weight loss around 160°C (2.1, 1.6 and 0.6% for Cu/Zr(3), Cu/Zr(7) and Cu/Zr(10) respectively.) is likely due to moisture evaporation, while the secondary weight loss after 500°C (1.7, 1.45 and 1.5% for Cu/Zr(3), Cu/Zr(7) and Cu/Zr(10) respectively.) might be due to the decomposition of any organic residues and potential impurities in the samples. The BET analysis (as shown in Figure S1) further supports the observations from the FT-IR, TGA, SEM, and TEM studies, shedding light on the effect of pH on the surface area and porosity of the synthesized CuO-ZrO2 nanocomposites. When the pH was increased from 3 to 10, the surface area decreased. This can be attributed to the acidic environment at lower pH (e.g., pH 3), which likely leads to reduced particle aggregation and consequently, a higher surface area. In contrast, at higher pH (e.g., pH 10), a more basic environment tends to promote the formation of larger particles or agglomerates, thereby reducing the surface area.

Among the samples, Cu/Zr (7) showed the highest pore volume of 0.124 cc/g (Table 1). This could be a result of the balanced interactions between the metal oxides at neutral pH. The neutral pH (pH 7) might favour the formation of a more porous structure compared to acidic or basic conditions, offering optimal conditions for pore formation.

Nanocomposites	Surface area (m ² /g)	Pore Volume (cc/g)	Pore Diameter (nm)
Cu/Zr(3)	48.90	0.062	37.28
Cu/Zr(7)	45.03	0.124	31.02
$C_{11}/Z_{r}(10)$	6.34	0.017	31 14

Table 1. Comparative Study of the Surface area, Pore Volume and Pore Diameter of prepare NPs.

In comparison, both acidic and basic conditions may disrupt these interactions, leading to less porosity [30]. The enhanced pore volume in Cu/Zr(7) is critical for improved photocatalytic activity, as it provides more active sites for the adsorption and consequently degradation of both RB and BB dyes, which is discussed in further sections of this study.

The general surface morphology of the better performing Cu/Zr (7) nanocomposite was examined by SEM and TEM techniques. The SEM images revealed high-density growth of the material (Figure 3 A), while TEM images highlighted the formation of nanomaterial agglomerates with irregular shapes (Figure 3 B) and lattice fringes oriented in various directions, confirming their polycrystalline nature and the presence of multiple phases within the crystal structure, consistent with the XRD data (Figure 3 C).

In order to confirm the formation of CuO-ZrO₂ nanocomposites and analyse their elemental composition, EDS analysis was performed. EDS spectra obtained from various locations confirmed the presence of Zr, Cu and O with variable atomic % depending on the preparation pH of the samples (Table S2). The average particle size of the synthesised nanocomposite was calculated by ImageJ software and was ~ 9.71 nm (Figure 3 D).

Also, the optical and electronic structural properties of the synthesized Cu/Zr (7) nanocomposites were investigated using UV-Vis reflectance spectroscopy, and the energy band gap (E_g) was calculated to be 2.4 eV using the Tauc plot (Figure 3 E). This relatively narrow band gap is crucial for enabling efficient absorption of visible light, making the Cu/Zr(7) nanocomposite highly suitable for photocatalytic applications. The Band gap Comparison for CuO, ZrO₂ and nanocomposite CuO-ZrO₂ is shown in Figure S2. Coupled with its polycrystalline structure, surface functional groups, and high pore volume, these attributes position the nanocomposite as a promising material for dye degradation, a potential explored further in this study.

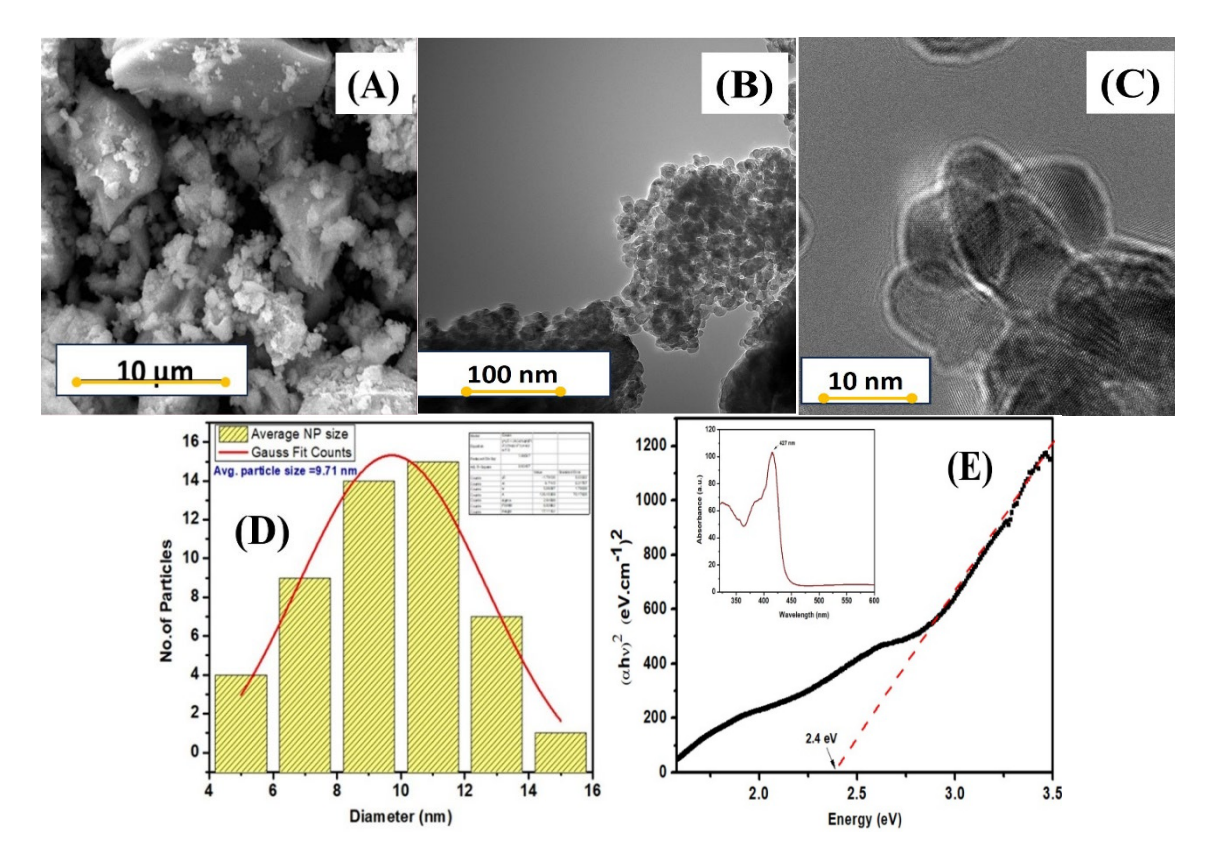


Fig. 3. (A) SEM analysis for the morphology (B/C) TEM analysis, (D) average particle size and (E) Band gap analysis of the Cu/Zr(7) nanocomposite.

3.2. Photocatalytic performance of CuO-ZrO₂ nanocomposites: effect of the synthesis pH

The degradation and removal efficiencies of the CuO-ZrO₂ nanocomposites synthesized at the different pH levels of 3, 7, and 10 (namely, Cu/Zr(3), Cu/Zr(7) and Cu/Zr(10)) were carried out at pH 4, 7 and 12 for both the dyes and the best results were obtained for RB dye at pH 4 and BB dye at pH 12. The experimental data, illustrated in Figure 4 (A,B), reveal a significant variance in performance based on the synthesis pH of the nanocomposites.

Among the tested samples, the Cu/Zr(7) exhibited the highest percentage of degradation for both dyes. The superior photocatalytic activity of the Cu/Zr(7) nanocomposite can be attributed to its optimal structural features, as highlighted in all the characterization results above.

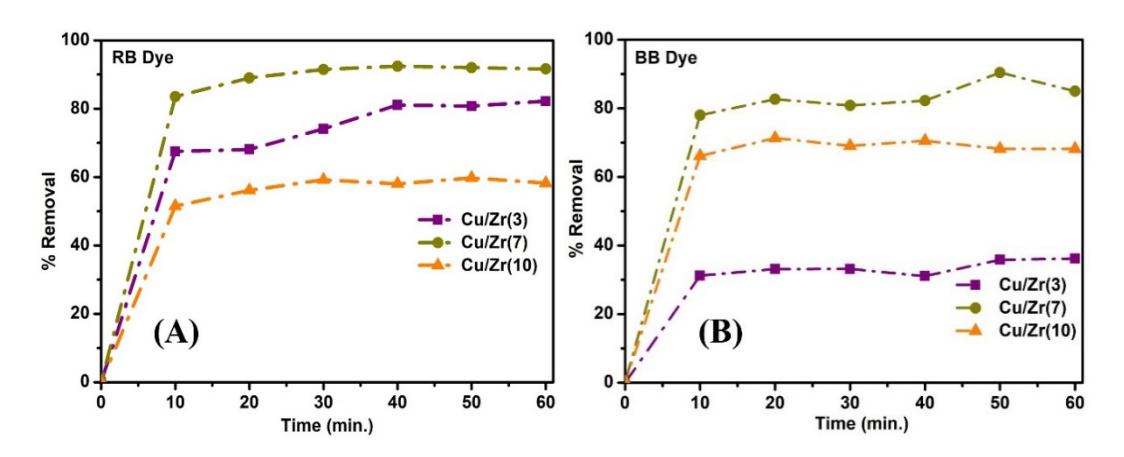


Fig. 4. Comparison studies for removal efficiency of the prepared CuO-ZrO₂ nanoparticles for (A) RB dye and (B) BB dye.

The Cu/Zr (7) nanocomposite exhibited a relatively narrow band gap of 2.4 eV, allowing for efficient visible light absorption, and its high surface area and pore volume provided ample active sites for dye adsorption. Moreover, the interaction between CuO and ZrO₂ nanoparticles, evidenced by lattice fringes and polycrystalline structures in TEM images, played a crucial role in enhancing charge separation and light absorption, leading to the generation of more photogenerated electrons and holes for photocatalytic reactions. FT-IR analysis also confirmed the presence of functional groups conducive to adsorption, further facilitating dye removal.

In addition, among the synthesized nanocomposites, the Cu/Zr(7) displayed the highest pore volume, which likely contributed to an extended contact time between the nanocomposite and the dye molecules. This prolonged interaction is crucial for facilitating optimal degradation efficiency.

These findings underscore the significant impact of synthesis pH on the structural and functional properties of the nanocomposites, thereby affecting their interaction with different dye molecules under varying pH conditions. Based on these findings, the Cu/Zr(7) nanocomposite was selected for further in-depth studies on dye degradation and environmental safety similar to the findings in other work[30].

3.3. Factors affecting the photocatalytic degradation of model dyes 3.3.1. Effect of pH of dye solutions

Maintaining consistent reaction parameters and concentrations, the prepared Cu/Zr(7) nanocomposites were examined for their efficiency in removing both the model RB & BB dyes. Firstly, the influence of the pH of the reaction medium was examined at room temperature, with a fixed amount of photocatalyst added to 20 mL of a solution containing 25 ppm of each dye. To investigate the pH dependence of both the dyes, three pH levels were selected: 4 (acidic), 7 (neutral), and 12 (alkaline).

The study demonstrated significant variation in adsorption efficiency with pH. For RB dye the highest removal capacity of ~ 92 % with C/C₀= 0.09624 was observed at pH 4, whereas the removal capacity at pH 12 was comparatively lower (~ 50.8 % and C/C₀ = 0.53) (Figure 5 A). At acidic pH, the surface of the nanocomposite may become positively charged due to the protonation of surface functional groups. This positive charge enhances the electrostatic attraction between the nanocomposite and the negatively charged RB dye molecules as they are likely to exist in their anionic form in an acidic medium [36], [37]. This interaction leads to enhanced photocatalysis and consequently, dye removal. In contrast, for BB dye, the removal capacity increased with higher pH, reaching a value of ~ 76 % at pH 12 (Figure 5 B). At alkaline pH, the surface of the nanocomposite is likely negatively charged due to the deprotonation of surface groups, which enhances the electrostatic attraction between the negatively charged nanocomposite surface and the positively charged BB dye molecules [36], [38]. Additionally, the higher availability of hydroxyl ions at alkaline pH promotes the generation of hydroxyl radicals further improving the degradation of BB dye.

3.3.2. Effect of catalytic dosages

Further, to study the loading effects of Cu/Zr (7) nanocomposites on the removal efficiency, several tests were conducted with varying nanocomposites dosages, from 10 to 60 mg in 20 mL of 25 ppm dye solutions (Figure 5 C, D). The results showed that the dye removal efficiency improves with increasing nanocomposite dosages, attributed to the larger available surface area providing more active sites for interaction with the dye molecules. When the dosage exceeded 30 mg, there was no significant further increase in dye removal efficiency but a slight decrease in efficiency at the end of 60 mins. This suggests that beyond this amount, the additional nanocomposites do not contribute to the photocatalytic activity, likely due to the saturation of active sites or possible aggregation effects [39] caused by the nanocomposite itself.

3.3.3. Effect of dye concentrations

Figures 5 (E, F) illustrated the variation of normalized concentration (C/C_0) of Reactive Black (RB) and Bismarck Brown (BB) dyes, respectively, over time for different initial dye concentrations (10, 15,25 and 30 ppm).

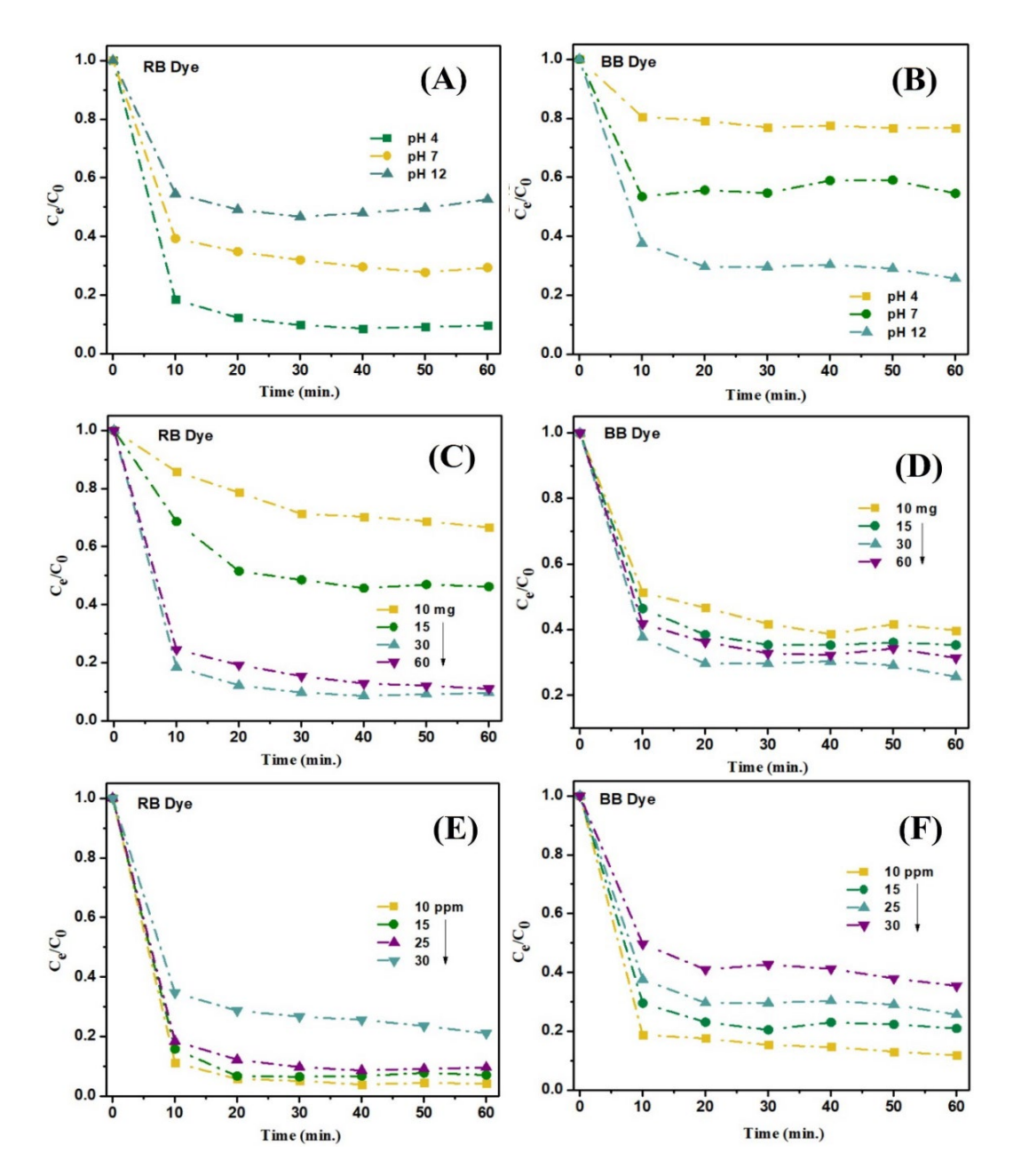


Fig. 5. (A/B) Comparative analysis of dye removal at different pH 4, 7, and 12 (C/D) effects of the NP dosage concentration on dye removal (E/F) effects of model dye concentration.

For both the dyes, a significant decrease in C/C_0 was observed during the initial 10-15 mins of reaction time, indicating rapid degradation during the early phase due to high availability of active sites on the photocatalyst surface.

The results clearly indicated that the photocatalytic efficiency decreases with increase in initial dye concentration. As the concentration increases from 10-25 ppm, the degradation becomes slower, but still effective. The degradation performance after 25 ppm is more important, particularly for BB dye (Figure 5 F).

This suggested a threshold beyond which the catalyst's efficiency drops considerably, likely due to both light shielding effects and competitive adsorption among dye molecules and intermediated species [40].

However, a further increase to 30 ppm results on a notably reduced degradation rate. This decline in the removal efficiency can be due to reduction of penetration of light and thereby decreasing photon adsorption by photocatalyst. Additionally, excess dye molecules can saturate the surface active sites of the photocatalyst, leading to lower reaction rates [41].

3.3. Kinetic study and isotherms

The adsorption performance of the Cu/Zr(7) nanocomposite towards Reactive Black (RB) and Bismarck Brown (BB) dye was systematically evaluated through isotherm and kinetic modelling.

Among the tested models, the Langmuir isotherm demonstrated the best fit for both the dyes, with high correlation coefficients (R^2 = 0.98935 for RB and 0.98044 for BB), indicating monolayer adsorption on a homogeneous surface with finite, energetically equivalent adsorption sites [42].

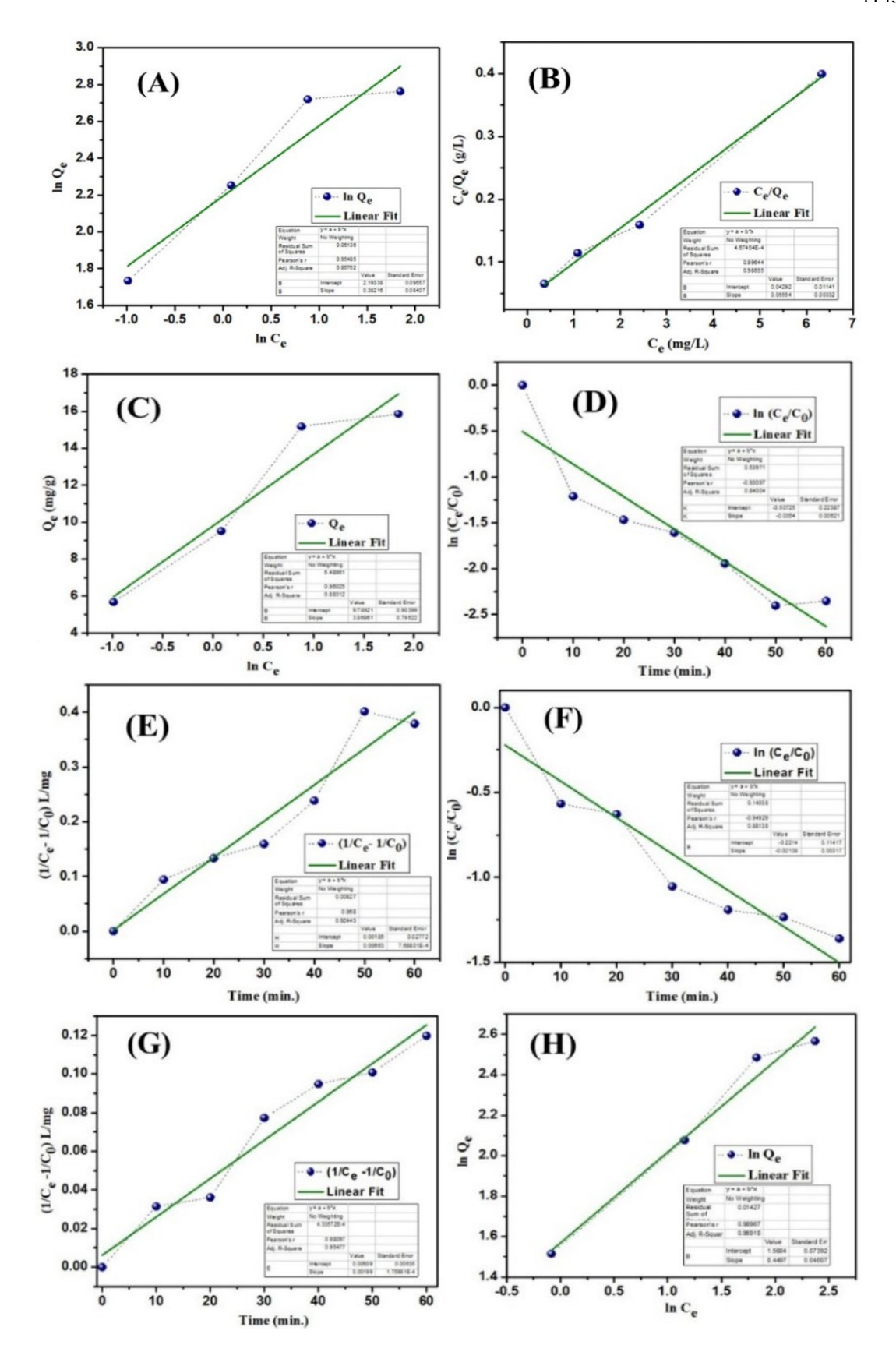
The Freundlich and Temkin models yielded comparatively lower R² values (RB: 0.86765 and 088312; BB: 0.96918 and 0.95456, respectively), implying the secondary presence of multilayer adsorption on heterogeneous sites [43].

Further, the kinetic analysis revealed that the pseudo-second order model provided a superior fit ($R^2 = 0.92443$ for RB and 0.95477 for BB), suggesting that chemisorption governed the rate-limiting step for dye removal [44].

These findings (Table 2) confirmed that the CuO-ZrO₂ i.e. Cu/Zr (7) exhibited consistent and efficient dye adsorption and removal, primarily following Langmuir-type monolayer adsorption and second order kinetic. (Figure 6 A-J).

Table 2. Isotherm models and kinetic parameters for the degradation of RB and BB dyes.

	Parameters	Values	
Isotherm model/ Kinetics		RB	BB
	K _F (L/g)	8.97	4.80
Freundlich	1/n	0.381	0.45
	\mathbb{R}^2	0.86765	0.96918
	Q _e (mg.g ⁻¹)	18.01	16.40
Langmuir	$K_L (L.mg^{-1})$	1.29	0.37
	\mathbb{R}^2	0.98935	0.98044
	B (j. mole ⁻¹)	32.16	30.01
Temkin	$K_{T}(L/g)$	12.56	3.59
	\mathbb{R}^2	0.88312	0.9545
	K ₁ (1/min)	0.0354	0.02138
Pseudo- First order	Q _e (mg.g ⁻¹)	0.602	0.80
(linear)	\mathbb{R}^2	0.84004	0.8814
	K ₂ (g/ mg.min)	0.02376	0.00065
Pseudo-second order	$Q_e (mg.g^{-1})$	150.83	502.51
(linear)	\mathbb{R}^2	0.92443	0.95477



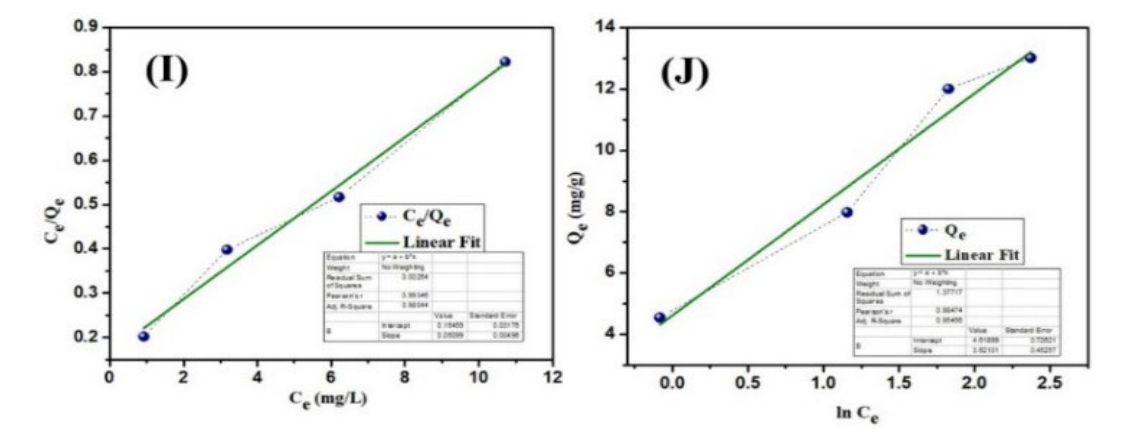


Fig. 6. (A/B/C) Freundlich, Langmuir and Temkin isotherm for RB dye (/D/E) first and second order kinetics for RB dye (F/G) first and second order kinetics for BB dye (H/I/J) Freundlich, Langmuir and Temkin isotherm for BB dye.

3.4. Trapping experiments for active species

Trapping experiments were conducted to identify the key reactive scavengers involved in the dye degradation mechanism, as the interactions between the photocatalyst and reactive species play a crucial role in this process. Typically, the primary active species responsible for the photooxidation of contaminants include holes (h⁺), superoxide (O_2 -), hydroxyl (.OH), and electron (e⁻) radicals [30], [45]. To clarify the photocatalytic mechanism of both RB and BB dyes by the CuO-ZrO₂ nanocomposites, degradation studies were carried out with Cu/Zr (7) employing EDTA, ascorbic acid, IPA, and $K_2Cr_2O_7$ as radical scavengers to capture these active species like holes (h⁺), superoxide (O_2 -), hydroxyl (OH) and electron (e⁻) radicals respectively. As shown in Figure. 7, the degradation efficiency decreased in the following order: $K_2Cr_2O_7 > EDTA > ASC > IPA$ for RB dye and EDTA > $K_2Cr_2O_7 > ASC > IPA$ for BB dye (Figure 7 A,B). Since the presence of $K_2Cr_2O_7$ and EDTA severely affected the photocatalytic degradation of both RB and BB dyes, it can be concluded that the generated e⁻ and h⁺ were the primary active species and played a major role in the degradation processes.

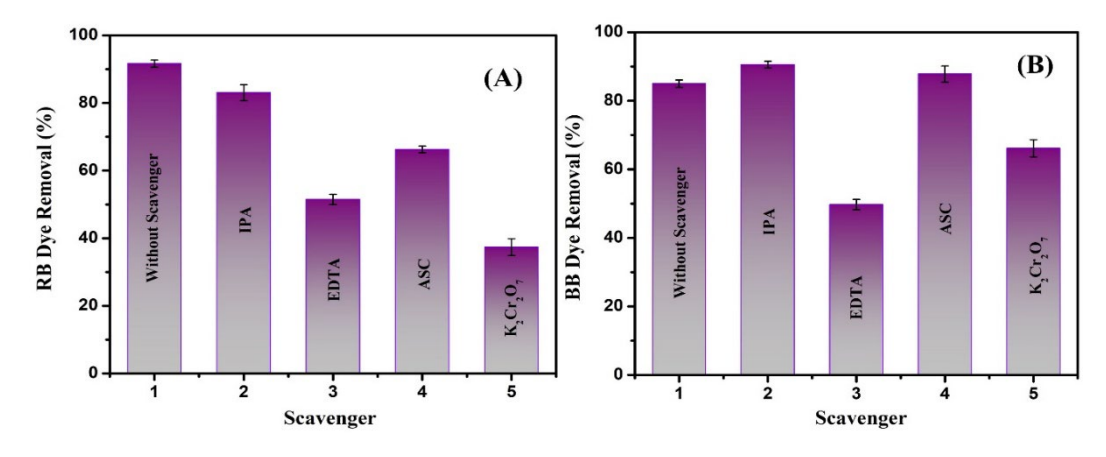


Fig. 7. The effect of scavengers on the degradation of (A) RB dye and (B) BB dye using Cu/Zr(7) nanoparticles.

3.5. Mechanism

3.5.1. Photocatalyst activation

CuO and ZrO₂ combine to form a heterojunction photocatalyst, where CuO serves as a narrow-bandgap semiconductor (capable of absorbing visible light), while ZrO₂ improves charge

separation and stability. When exposed to light, the Cu/Zr(7) photocatalyst becomes activated, potentially generating electron-hole pairs (Equation 2) [46]:

$$CuO/ZrO_2 + hv \rightarrow e^-(CB \text{ of } CuO) + h^+(VB \text{ of } CuO)$$
 (Equation 2)

The ZrO₂ in the nanocomposite also helps to reduce electron-hole recombination by facilitating the migration of charges, allowing the electrons and holes to remain available for subsequent redox reactions. This enhanced charge separation and transfer significantly improve the photocatalytic efficiency, promoting the degradation of organic contaminants during the photocatalysis process.

3.5.2. Formation of reactive species

Once the photocatalyst is activated, reactive oxygen species (ROS) are generated, a common feature in photocatalytic systems [47]. As seen in the active species trapping experiments, the e^- and h^+ are the primary active species in the degradation of both model dyes. Electrons in the conduction band (CB) have significant reductive power, reducing dissolved oxygen molecules (O₂), resulting in the formation of superoxide anions (O₂ $^{-}$ •) (Equations 3 and 4)[48], [49].

$$e^-+O_2 \rightarrow O_2^-$$
 (Equation 3)

$$O_2^-$$
 + dye molecules \rightarrow Degradation products (Equation 4)

These superoxide anions $(O_2^{-\bullet})$ play a crucial role in breaking down and can attack the dye molecules, leading to the formation of smaller degradation products. Meanwhile, the positively charged holes (h^+) can directly oxidize the dye molecules by attacking their chromophore structure and initiating degradation. The holes can also oxidize water (H_2O) molecules or hydroxide ions (OH^-) to generate hydroxyl radicals $(\bullet OH)$, which are highly reactive species that further attack the dye, enhancing the degradation process (Equations 5 and 6) [48], [49]:

$$h^+ + H_2O \rightarrow OH + H^+$$
 (Equation 5)

$$\cdot$$
OH+ dye molecules \rightarrow CO₂+H₂O (Equation 6)

For RB dye, the low concentration of hydroxide ions (OH) at pH 4 limits the generation of •OH, making water oxidation only primary pathway for •OH generation. Hence, the active species trapping experiment for RB dye showed that the •OH radicals had minimal influence on RB dye degradation. In contrast, at pH 12 for the BB dye, the higher concentration of hydroxide ions (OH) increases the formation of the •OH radicals. These radicals, produced by the interaction of hydroxide ions with photogenerated holes, play a major role in the photocatalytic degradation of the BB dye, contributing to its more efficient removal at higher pH.

Additionally, recyclability studies (Fig. S3) were also performed with 25 ppm dye solutions using 30 mg of the Cu/Zr (7) nanocomposite. After each cycle, the used nanocomposite was washed with double distilled water, dried overnight at 60 °C and reused under the same experimental settings. It is noteworthy that the nanocomposite did not show any obvious loss of activity up 3 cycles for RB dye and up to 4 cycles for BB dye with just over all decrease of ~12.69% for RB and ~16.5% for BB dye by the end of 5 cycles (Figure S3), implying its stable photocatalytic activity with exceptional reusability without the loss of catalytic properties.

3.6. Ecotoxicological profiling

The phytotoxic effects of the Cu/Zr (7) nanocomposites were assessed through a seed germination test on the *V. radiata* (green grams) seeds (Figure 8) [31] over a 3-day period. Mean Root length (MRL), Germination Index (GI), and Root Growth Inhibition % were calculated for concentrations of 25, 50, 75, and 100 ppm, compared to the untreated control. The MRL of the

control group was observed to be 7.92 cm, while treatments at 25 and 50 ppm yielded longer average root lengths of 10.28 cm and 10.24 cm, respectively. The corresponding calculated inhibition percentages were -29.80% and -29.29% (Figure 8), indicating a clear positive stimulatory effect on root growth at lower concentrations. The negative inhibition values can be taken as indicative of hormesis, a biphasic dose-response phenomenon where low concentrations of potentially toxic agent induces a stimulatory or beneficial effect on biological systems [50] [51]. In this case, the nanoparticles appeared to act as micronutrient enhancer at sub-toxic concentrations. However, at higher concentrations of 75 ppm and 100 ppm, root growth declined significantly, with inhibition percentages turning positive (e.g., 100 ppm showed a 26.52% inhibition), thus indicating phytotoxic stress. These findings highlighted in Table 3 showed the dualistic role of the Cu/Zr (7) NPs that while across all the treatments, the germination % was 100% and unaffected, post-germination root development was sensitive to the NPs concentration.

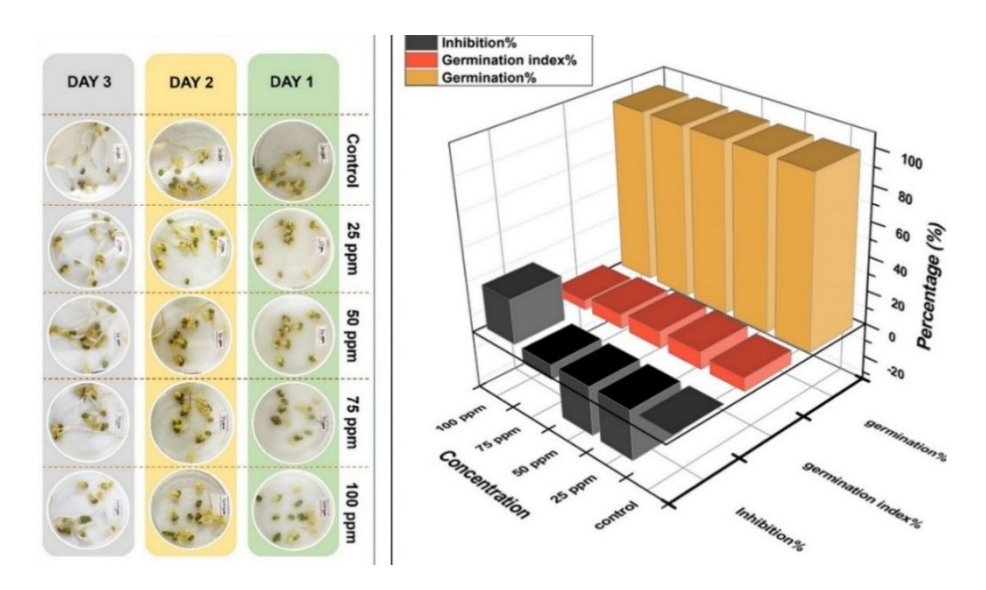


Fig. 8. Seed germination assay.

Germination % Mean Root Length Inhibition % Concentration Germination Index (ppm) (cm) % 0 (Control) 100 7.92 7.92 0 25 ppm 100 10.28 10.28 -29.8 10.24 -29.3 50 ppm 100 10.24 100 8.62 8.62 75 ppm -8.8 100 ppm 100 5.81 5.81 26.6

Table 3. Seed germination measurements.

However, it is important to note that to comprehensively assess the environmental impact of these nanocomposites, further toxicity studies with different model organisms and under varying conditions are necessary. These additional experiments would provide a more complete understanding of the potential long-term effects and safety of the nanocomposites in diverse environmental contexts.

4. Conclusion

In this study, we successfully synthesized a novel Cu/Zr(7) nanocomposites using a simple, cost-effective method demonstrating significant efficiency in degrading both cationic and anionic dyes (RB and BB dyes) under visible light irradiation. The exceptional performance can be attributed to the synergistic effect of CuO and ZrO₂, where CuO absorbs visible light, and ZrO₂ facilitates charge separation, reducing electron-hole recombination. This synergism enables the efficient generation of reactive species responsible for improving the photocatalytic activity of the nanocomposites. The eco-friendly synthesis method and non-toxic nature of the photocatalyst were validated through ecotoxicological profiling, ensuring that the nanomaterial poses no harm to aquatic life and the environment via experiments with *V. radiata* seeds. Therefore, the prepared Cu/Zr(7) photocatalyst not only offers an efficient solution for dye degradation but also aligns with more sustainable principles, making it a promising candidate for wastewater treatment applications without adverse environmental impacts. Furthermore, the recyclability studies demonstrated excellent stability, with the photocatalyst retaining its activity over multiple cycles, highlighting its durability and cost-effectiveness.

Overall, the Cu/Zr(7) nanocomposite offers a sustainable and highly efficient approach to wastewater treatment, aligning with more sustainable principles. Its non-toxic nature and reusability position it as a promising candidate for practical applications in environmental remediation, contributing to sustainable water management solutions with minimal environmental impact. However, further studies on its long-term ecotoxicological effects across different organisms and environmental conditions and scalability are recommended to ensure broader safety and applicability.

Acknowledgements

The authors are grateful for the facilities and financial support provided by the Department of Physics, Panjab University, Commonwealth Scholarship Commission (CSC) and Queen Mary University of London, UK. The CSC scholarship was provided to K. Rajput (CSC No: INCN-2023-6).

References

- [1] A. S. Adeleye, J. R. Conway, K. Garner, Y. Huang, Y. Su, A. A. Keller, Chem. Eng. J., 286, 640, (2016); https://doi.org/10.1016/j.cej.2015.10.105
- [2] M. Caianelo, C. Rodrigues-Silva, M. G. Maniero, V. Diniz, M. Spina, J. R. Guimarães, Water Sci. Technol.,84 (1),225, (2021); https://doi.org/10.2166/wst.2021.208
- [3] V. Diniz, C. R. Crick, S. Rath, J. Environ. Manage., 346, 118979, (2023); https://doi.org/10.1016/j.jenvman.2023.118979
- [4] A. Chithambararaj, N. S. Sanjini, S. Velmathi, A. Chandra Bose, Phys. Chem. Chem. Phys., 15, (35), 14761, (2013); https://doi.org/10.1039/c3cp51796a
- [5] B. Senthil Rathi, P. Senthil Kumar, Curr. Opin. Green Sustain. Chem., 33, 100578, (2022); https://doi.org/10.1016/j.cogsc.2021.100578
- [6] A. Manivel et al., Mater. Res. Bull., 62, 184, (2015); https://doi.org/10.1016/j.materresbull.2014.11.016
- [7] A. S. Al-Wasidi, E. A. Abdelrahman, Discov. Nano, 18, (1), 97, (2023); https://doi.org/10.1186/s11671-023-03873-x
- [8] A. Khalid, M. Zubair, Ihsanullah, Arab. J. Sci. Eng., 43, (5), 2167, (2018); https://doi.org/10.1007/s13369-017-2543-x
- [9] U. M. Lekhak, Elsevier Inc., 45,(2023); https://doi.org/10.1016/B978-0-323-91235-8.00021-8
- [10] M. Alhamd, T. Tabatabaie, I. Parseh, F. Amiri, N. Mengelizadeh, Environ. Sci. Pollut. Res.,

```
28(40), 57099, (2021); https://doi.org/10.1007/s11356-021-14590-2
```

[11] A. H. Jawhari, M. A. Malik, N. Hasan, B. Fatima, J. Mol. Struct.,1305, 137594, (2024); https://doi.org/10.1016/j.molstruc.2024.137594

[12] N. M. Hosny, I. Gomaa, M. G. Elmahgary, Appl. Surf. Sci. Adv., 15, (February), 100395, (2023); https://doi.org/10.1016/j.apsadv.2023.100395

[13] I. Gehrke, A. Geiser, A. Somborn-Schulz, Nanotechnol. Sci. Appl., 8, (2015).

[14] H. Wang, P. Sun, L. Yin, X. Sheng, InfoMat, 2(3),527, (2020); https://doi.org/10.1002/inf2.12054

[15] H. Wu, H. N. Alshareef, T. Zhu, InfoMat, 1(3), 417, (2019); https://doi.org/10.1002/inf2.12022

[16] X. Qu, P. J. J. Alvarez, Q. Li, Water Res., 47(12), 3931, (2013); https://doi.org/10.1016/j.watres.2012.09.058

[17] J. Yu, R. Chen, InfoMat, 2(5), 905, (2020); https://doi.org/10.1002/inf2.12106

[18] A. B. Djurišić, Y. H. Leung, A. M. Ching Ng, Mater. Horizons, 1(4), 400, (2014); https://doi.org/10.1039/c4mh00031e

[19] K. Rajput et al., Mater. Today Proc., 57, 846, (2022); https://doi.org/10.1016/j.matpr.2022.02.457

[20] G. Ghasemzadeh, M. Momenpour, F. Omidi, M. R. Hosseini, M. Ahani, A. Barzegari, Front. Environ. Sci. Eng., 8(4), 471, (2014); https://doi.org/10.1007/s11783-014-0654-0

[21] Y. Zhang, S. J. Park, Appl. Catal. B Environ., 240 (August 2018), 92, (2019); https://doi.org/10.1016/j.apcatb.2018.08.077

[22] G. Zhou et al., Nat. Commun., 9(1), 1, (2018).

[23] Y. Wu et al., Chem. Eng. J., 410 (December 2020), 128393, (2021); https://doi.org/10.1016/j.cej.2020.128393

[24] A. T. Jalil et al., J. Nanostructures, 11(2), 333, (2021).

[25] C. V. Reddy et al., J. Environ. Manage., 260(November 2019),110088, (2020).

[26] S. S. Batool, R. Saleem, R. R. M. Khan, Z. Saeed, M. Pervaiz, M. Summer, 178, 108419, (2024); https://doi.org/10.1016/j.mssp.2024.108419

[27] B. M. Alajmi, A. S. Basaleh, A. A. Ismail, R. M. Mohamed, Surfaces and Interfaces, 39(April), 102899, (2023); https://doi.org/10.1016/j.surfin.2023.102899

[28] M. Zain et al., Mater. Res. Express, 11(4), 045002, (2024); https://doi.org/10.1088/2053-1591/ad3db3

[29] R. Öztekin, D. T. Sponza, Chem. Sci. Int. J., 32 (2),1, (2023); https://doi.org/10.9734/CSJI/2023/v32i2845

[30] K. Rajput, K. J. Kaur, D. Devvrat, S. K. Mehta, S. Sareen, M. D. Sharma, Top. Catal., 67(9-12), 594, (2024); https://doi.org/10.1007/s11244-023-01897-2

[31] J. Kaur, K. Kaur, N. Pervaiz, S. K. Mehta, ACS Appl. Nano Mater., 4(11), 12766, (2021); https://doi.org/10.1021/acsanm.1c03433

[32] S. Huo, H. Zhao, J. Dong, J. Xu, Electroanalysis, 30 (9), 2121, (2018); https://doi.org/10.1002/elan.201800284

[33] M. Mn et al., 4, 1139, (2010).

[34] O. R. Rodig, J. Med. Chem., 6(6), 826, (1963); https://doi.org/10.1021/jm00342a059

[35] Z. Çetinkaya, Konya J. Eng. Sci., 8055, 221, (2024);

 $\underline{https://doi.org/10.37394/232014.2023.19.24}$

[36] M. Kosmulski, J. Colloid Interface Sci., 337(2), 439, (2009); https://doi.org/10.1016/j.jcis.2009.04.072

[37] M. Siddique, R. Khan, A. F. Khan, R. Farooq, J. Chem. Soc. Pakistan, 36(1), 37, (2014).

[38] C. Arab, R. El Kurdi, D. Patra, Mater. Chem. Phys., 277(March 2021), 125504, (2022); https://doi.org/10.1016/j.matchemphys.2021.125504

- [39] V. Mutreja, M. D. Sharma, K. Rajput, R. Sharma, S. K. Mehta, S. Sareen, Top. Catal., 65 (19-20),1963, (2022); https://doi.org/10.1007/s11244-022-01741-z
- [40] H. T. Nguyen, V. Doan, L. Huong, A. Nguyen, 15 (8),6241, (2025); https://doi.org/10.1039/D5RA00625B
- [41] H. Yu, J. Huang, L. Jiang, X. Yuan, K. Yi, 408, 127334, 2021; https://doi.org/10.1016/j.cej.2020.127334
- [42] R. Ranguin et al., Molecules, 30 (10),2096, (2025); https://doi.org/10.3390/molecules30102096
- [43] V. O. Shikuku, T. Mishra, Appl. Water Sci., 11 (6), 1, (2021); https://doi.org/10.1007/s13201-021-01440-2
- [44] Y. Guo, M. Ma, Q. Gong, G. Li, G. Zhou, 366, 1, (2025); https://doi.org/10.1016/j.seppur.2025.132772
- [45] N. Kumari et al., Top. Catal., vol. 65 (19), 1938, (2022); https://doi.org/10.1007/s11244-022-01735-x
- [46] S. Pal, S. Maiti, U. N. Maiti, K. K. Chattopadhyay, CrystEngComm, 17(6), 1464, (2015); https://doi.org/10.1039/C4CE02159B
- [47] M. Caianelo, J. C. Espíndola, V. Diniz, M. Spina, C. Rodrigues-Silva, J. Roberto Guimarães, J. Photochem. Photobiol. A Chem., 430, 113973, 2022; https://doi.org/10.1016/j.jphotochem.2022.113973
- [48] N. D. Khiavi, R. Katal, S. K. Eshkalak, S. Masudy-Panah, S. Ramakrishna, H. Jiangyong, Nanomaterials, 9(7),1011, (2019); https://doi.org/10.3390/nano9071011
- [49] V. Rani et al., Catalysis, 12(11), 1418, (2022); https://doi.org/10.3390/catal12111418
- [50] A. Chahardoli, Environ. Sci. Pollut. Res., 30(44), 100078, (2023); https://doi.org/10.1007/s11356-023-29359-y
- [51] R. Mireya, H. Herrera, G. Hernández, C. Mauricio, M. Ochoa, J. Appl. Phycol., 34 (4), 2187, (2022); https://doi.org/10.1007/s10811-022-02780-5